Mechanics of Advanced Materials and Structures

ISSN: 1537-6494 (Print) 1537-6532 (Online) Journal homepage: www.tandfonline.com/journals/umcm20

Comparative analysis of mechanical properties of porous structures obtained on the basis of triply periodic P-surfaces

M. A. Frolov, M. I. Smolkov, A. F. Krutov, A. V. Burchakov & V. A. Blatov

To cite this article: M. A. Frolov, M. I. Smolkov, A. F. Krutov, A. V. Burchakov & V. A. Blatov (17 Jun 2025): Comparative analysis of mechanical properties of porous structures obtained on the basis of triply periodic P-surfaces, Mechanics of Advanced Materials and Structures, DOI: 10.1080/15376494.2025.2518468

To link to this article: https://doi.org/10.1080/15376494.2025.2518468

Published online: 17 Jun 2025.

MECHANICS OF ADVANCED MATERIALS AND STRUCTURES
https://doi.org/10.1080/15376494.2025.2518468

Taylor & Francis
Taylor & Francis Group

ORIGINAL ARTICLE

Comparative analysis of mechanical properties of porous structures obtained on the basis of triply periodic P-surfaces

M. A. Frolov[a], M. I. Smolkov[b], A. F. Krutov[a], A. V. Burchakov[a], and V. A. Blatov[a]

[a]General and Inorganic Chemistry, Samara State Technical University, Samara, Russia; [b]Computational Geometry and Materials Science Lab, Povolzhskiy State University of Telecommunications and Informatics, Samara, Russia

ABSTRACT

This study explores the mechanical properties of porous structures derived from 15 triply periodic P-surfaces (TPS(P)) originally modeled on zeolite atomic frameworks. Elastic characteristics were computed for representative volume elements (RVEs) of these surfaces, revealing significant variations in elastic moduli and pronounced anisotropic behavior. From the RVEs of the most mechanically robust structures, larger-scale architectures were fabricated using PLA+ material *via* additive manufacturing (AM). These specimens underwent thorough mechanical characterization, integrating numerical simulations with experimental tests, including load curve analysis. Computational predictions showed strong alignment with experimental data. A key finding is that some structures exhibit compressive strength surpassing that of the base material, underscoring the exceptional load-bearing capacity of these engineered porous structures.

ARTICLE HISTORY
Received 13 May 2025
Accepted 5 June 2025

KEYWORDS
Triply periodic P-surfaces; porous material; topological and geometrical properties; additive manufacturing; mechanical properties

1. Introduction

Nowadays porous structures based on triply periodic surfaces (TPS) and triply periodic minimal surfaces (TPMS) with various topological and geometric parameters are being actively studied and utilized across diverse fields of science and engineering [1–15]. Such structures exhibit remarkable mechanical [1–5], thermal-conductive, and hydrodynamic properties [6,7], as well as the ability to absorb deformation energy [8,9]. The literature actively discusses the use of periodic porous structures in biomedicine for bone implant applications (see, e.g. [10–13]). Porous structures based on TPS/TPMS can serve as an excellent foundation for creating interpenetrating phase composites (IPCs) [14,15] as well as metamaterials [16–19]. Triply periodic TPS/TPMS-based structures have gained particular importance due to advancements in additive manufacturing (AM), which enables their integration into numerous engineering solutions, thereby increasing interest in their theoretical and experimental investigation [8,11,14,17,18]. It should be noted that AM has naturally evolved into so-called 4D printing with the use of shape memory materials. In this regard, we highlight the studies [20,21], which investigate the influence of external conditions and printing parameters on the shape memory properties of samples made from PLA-based plastics.

A broader adoption of TPS/TPMS-based porous structures is hindered by the limited number of known TPS configurations, despite their long research history [22]. Typically, studies and applications focus on a very narrow range of TPS/TPMS (e.g. [10]). This limitation underscores the need to develop new methods for generating TPS with diverse topological and geometric properties (see, e.g. [23]). Among recent studies focusing on the development of new TPS/TPMS structures, we highlight in Felix et al., Yu. Arsentev et al., and Castañeda et al. [23–26].

Recently [27,33], we proposed a novel approach to design porous structures based on TPSs derived from topological network representations of crystalline chemical compounds, in particular zeolites [28] and metal-organic frameworks (MOFs) [29]. Based on the relations between TPSs and crystal structures [30], this method allows generating an infinite set of TPSs and the corresponding porous materials using periodic network templates and the ToposPro software package [31]. Once a surface has been given finite thickness, it can be fabricated *via* 3D printing, and its physical properties can be simulated using standard computational tools like ANSYS [32] or investigated experimentally. Our method is based solely on the geometric and topological properties of periodic networks [27,33] and can be applied to frameworks with nonstandard nodes, enabling the use of both real crystal structures and a wide array of artificially designed networks as templates for generating TPSs.

The method developed in Smolkov et al. [27,33] was applied to analyze the atomic frameworks of 253 zeolite crystals. From this set, 98 TPS/TPMS and a corresponding number of porous structures were obtained, differentiated by topological type, genus, space group symmetry, labyrinth network topology, Hopf network topology, and balance property [33]. It should be noted that the most widely used

CONTACT M. I. Smolkov m.smolkov97@gmail.com Computational Geometry and Materials Science Lab, Povolzhskiy State University of Telecommunications and Informatics, Samara, Russia.

TPMS in current literature are surfaces such as the *primitive surface* (Schwarz P), *gyroid surface* (Schwarz G), and *diamond surface* (Schwarz D). Within the entire collection of surfaces derived from zeolite atomic frameworks, we identified 15 surfaces as *primitive surfaces* (P-type), which will be referred to as TPS(P). In this work, we focus on a comparative analysis of the mechanical properties of porous structures based on these 15 surfaces, leaving surfaces of other types beyond the scope of our study. Notably, this set of P-surfaces includes both novel configurations and well-known structures such as the widely used Schwarz P-surface (see, e.g. [10]), which was obtained in our approach through topological analysis of the sodalite crystal lattice and is designated as SOD.

All TPS(P)s in this study share several key characteristics prior to smoothing:

i. They are composed of planar quadrilaterals and hexagons (4- and 6-membered rings).
ii. They possess identical dual labyrinth network topologies (**pcu**).
iii. They have a genus of 3.
iv. They are balanced surfaces.

The surfaces differ primarily in their derivation from atomic lattices of varying symmetry – ranging from monoclinic to cubic systems.

In this study, we employ ANSYS to compute mechanical properties of TPS(P)-based porous structures, specifically:

i. Effective values of elastic compression moduli.
ii. Shear moduli.
iii. Poisson's ratios.
iv. Their dependence on relative density *via* the Gibson-Ashby scaling law [34].
v. Von Mises stress distribution across the structures.
vi. Distribution of the third invariant of the stress tensor.

The calculated properties are compared with those of the Schwarz P-surface (SOD), with particular attention to surfaces exhibiting extreme mechanical characteristics. Next, more complex porous structures were assembled from the representative volume elements (RVEs) of the selected configurations with optimal properties. These structures were fabricated using PLA+ material *via* 3D printing for experimental measurement of compression moduli and derivation of corresponding stress-strain curves. The measured mechanical properties of the complex porous samples were then compared with those of structures commonly used in contemporary research.

The article is structured as follows. Section 2 provides a concise description of the methodology for generating triply periodic networks using the ToposPro software package, along with the technique and Porous 3D software for creating the corresponding TPS structures with finite thickness in formats to be suitable for 3D printing. Section 3 is devoted to the numerical modeling of effective elastic moduli of TPS(P) elementary cells used in this study. Section 4 simulates the mechanical properties of more complex samples of porous structures assembled from TPS(P) unit cells with extreme mechanical properties, which are made of PLA+ plastic. Section 5 presents the results of experimental studies of samples from Section 4, manufactured using additive technology. The Conclusion summarizes the key findings of the study.

2. Triply periodic surface generation

Recently [27], we introduced a universal method designed to generate TPSs, which can be applied to any periodic lattice of crystal structures that admits a *natural tiling*. The main idea of the method is to use crystals as natural periodic templates for TPSs. The atomic structures of some crystals have configurations similar to the labyrinth networks of TPSs (e.g., the atomic lattice of sodalite, see Figure 1).

The atomic network of such crystal decorates the corresponding TPS, and we find the decoration through constructing tiling [35], which represents a partitioning of the crystal space into generalized polyhedra (tiles) that fill this space without gaps or self-intersections. The faces of the tiles are formed by rings of the atomic network; hence, the tiles can be non-convex and can contain two-coordinated vertices [36]. Out of all possible tilings, the so-called *natural tiling* can be identified [37], in which the tiles are minimal, i.e. they cannot be split to smaller tiles. Such *natural tiles* act as fundamental building blocks for constructing larger tiles. Using this method, 98 TPSs based on zeolite crystal structures were generated [27]. Their topological descriptors were calculated revealing 55 distinct topological classes of surfaces. Among these, 12 surfaces were found to be isomorphic to already known TPMSs, while four out of the 98 surfaces represented new TPMSs. Additionally, 39 surfaces, though not minimal, were classified as TPSs.

Interestingly, several zeolites enabled generating 15 TPSs to be geometrically and topologically resembling the Schwarz P-surfaces. The resulting TPSs can be categorized into three subclasses (Table 1, Figure 2). The *P* class

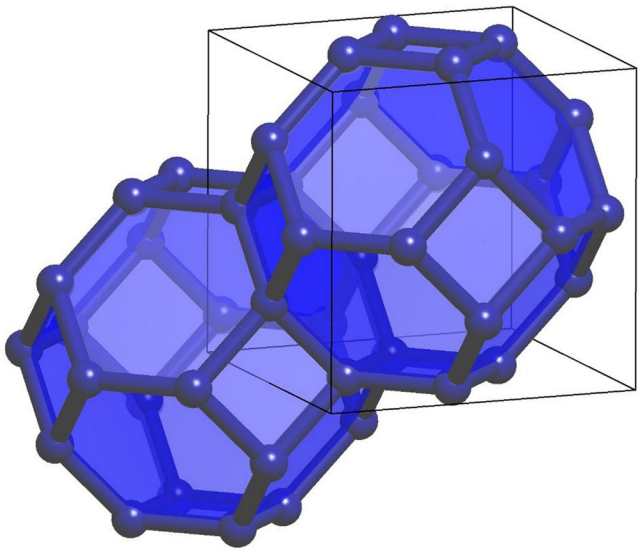

Figure 1. Atomic lattice of SOD zeolite (sodalite).

Table 1. Schwarz P-Surfaces subclassification by their geometrical parameters.

P-type	Zeolites (Figure 2)
Schwarz *P*	SOD (Sodalite), RHO (Rhodenite).
P-like ($\tilde{P}$)	LTA (Linde Type A), ATN (MAPO-39).
P-disp ($\tilde{P}_D$)	MER (Merlinoite), SAS (STA-6), BCT (Mg-BCCT), JSW (CoAPO-CJ62), HEU (Heulandite), CGF (Cobalt-Galiium-Phosphate-5), ITW (ITQ-12), EDI (Edingtonite), UEI (Mu-18), BRE (Brewsterite), LAU (Laumontite).

The *P* class represents surfaces that align with the classical Schwarz classification, the *P*-like class united surfaces that bear a resemblance to *P* surfaces but can undergo compression or stretching, *P*-disp class is a set of surfaces which are topologically identical to *P* surfaces yet they have different unit cells because these unit cells are extracted from another segment of an infinite triply periodic structure.

represents surfaces that align with the Schwarz classification. $\tilde{P}$ (*P*-like) surfaces are those that bear a resemblance to *P* surfaces but can undergo transformations such as compression or stretching. Meanwhile, $\tilde{P}_D$ (*P*-disp) surfaces are topologically identical to *P* surfaces, yet they have different unit cells because these unit cells are extracted from different segments of the same infinite triply periodic structure and these surfaces can also undergo transformations.

We follow the three-step workflow proposed in [33], schematically shown in Figure 3:

1. *Generation*: TPSs are computationally generated *via* ToposPro [31]. Using previously discussed network approach and net partitioning into natural tiles TPS generation is achieved by removing some tile faces under three conditions: all nodes and edges must lie on the TPS (*decoration condition*); each edge is shared by exactly two remaining faces (*edge condition*); edges meeting at a node belong to different face pairs (*node condition*). All valid face-removal combinations are and archived in the .t3g file format (Figure 4).
2. *Processing and refinement*: The TPS models undergo spatial adjustments, smoothing, and thickening (Figure 5) using Porous 3D [38] algorithms, with the final output exported as an .stl file for further use. Spatial adjustments incorporate a model translation algorithm. To generate an infinite TPS, the method analytically implements parallel translation in a rectangular coordinate system, enabling seamless boundary connections between adjacent unit cells. The facet smoothing algorithm combines Laplacian and optimization-based approaches to minimize the difference between maximum and minimum mean curvature values across surface mesh vertices, achieving TPMS-like smoothing. Mean curvature calculation employs Delaunay triangulation and normal cycle theory from differential geometry [39]. Surface thickening algorithm creates volumetric structures by offsetting the surface by a specified thickness.
3. *Analysis and validation*: The porous material model is either simulated in ANSYS [32] to evaluate its physical properties or fabricated *via* 3D printing for the subsequent experimental investigation.

3. Effective elastic moduli of TPS(P) unit cells

For the comparative investigation of mechanical properties in TPS(P) porous structures, we computed the compression moduli, shear moduli, and Poisson's ratios of their unit cells (Figure 2) under multidirectional loading, along with von Mises stress distribution analysis. Each TPS(P) structure was constructed by tessellating the unit cells along three orthogonal directions, with all unit cells designed within a $20 \times 20 \times 20$ mm cubic envelope and featuring 2 mm wall thickness. The digital twins of these unit cells were converted into RVEs.

The ANSYS [32] simulations employed structural steel [40] as the model material due to its well-defined linear elastic properties (Table 2), using finite element (FE) methods, which are commonly used for the calculation of mechanical properties of porous structures (e.g. [41]). In our work, the FE method incorporated Dirichlet periodic boundary conditions. Loading was applied through prescribed displacements equivalent to 3% of the corresponding RVE dimension. We utilized SOLSH190 continuum solid elements with 8-node connectivity and three degrees of freedom per node [32]. These conditions were selected for their capability to handle geometric nonlinearity while maintaining uniform mesh distribution that is a critical requirement for accurate elastic property analysis. The multi-zone meshing approach generated quadrilateral elements with a characteristic size of 1.7 mm throughout the models.

The simulated effective elastic properties of the TPS(P)-based porous structures are presented in Table 2. Our analysis revealed that all of them demonstrated maximum stiffness when compressed along the *z*-axis direction, while exhibiting their lowest compression modulus under *x*-axis loading. Notably, the *z*-axis compression moduli significantly mostly exceed those of the commonly used porous structure based on the Schwarz P-surface (labeled SOD in our approach as derived from the sodalite atomic network [23]). The averaged compression moduli along the remaining two principal directions also surpass the corresponding values for the Schwarz P-surface structure. The analysis of Poisson's ratios (Table 2) identifies the ATN, BRE, and LAU TPSs with anomalously high values exceeding 0.5.

We calculated the Pearson, Spearman, and Kendall correlations between the values of mechanical parameters in Table 2 and topological-geometrical characteristics of the porous structures. All correlations were rather weak ($r < 0.5$). This result indicates that reliable correlations between topological-geometric characteristics and mechanical properties in TPS/TPMS-based porous structures may require alternative descriptors more intrinsically related to the surface geometry and topology [42].

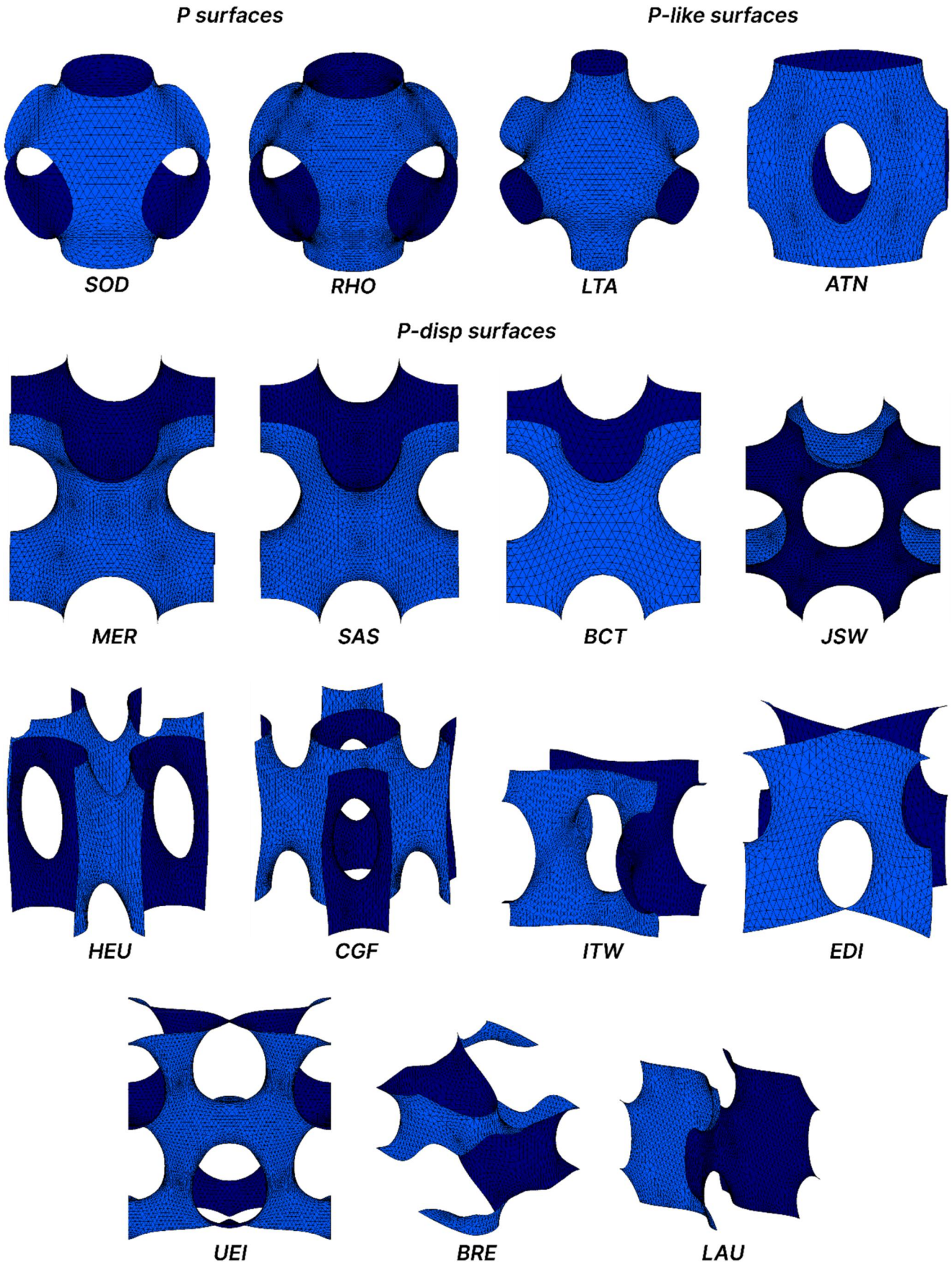

Figure 2. Unit cells of 15 TPS(P)s from Table 1 obtained from zeolites.

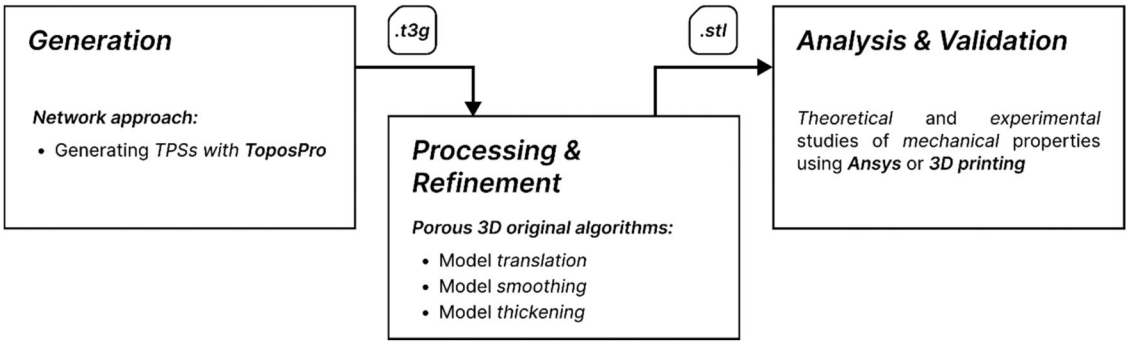

Figure 3. The computational workflow for modeling porous materials, as implemented in reference [33].

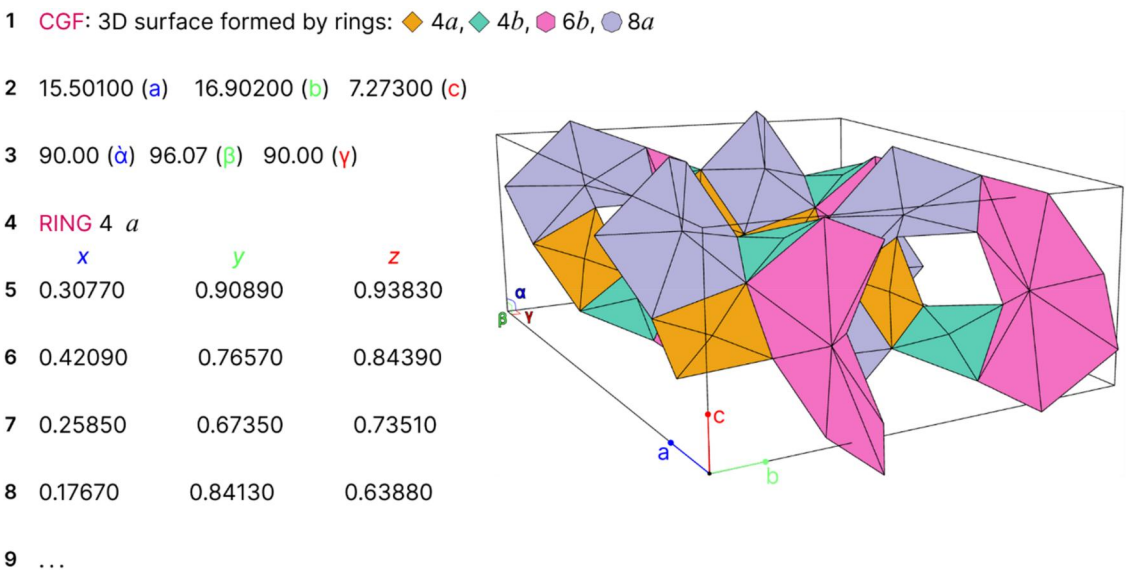

Figure 4. t3g File generated by ToposPro for TPS represented by eight (4a) and eight (4b) different independent 4-membered, eight (6b) 6-membered, and four (8a) 8-membered rings of periodic net obtained from Co-Ga-P-5 zeolite (CGF) crystal structure as well as the dimensions and angular parameters of unit cell.

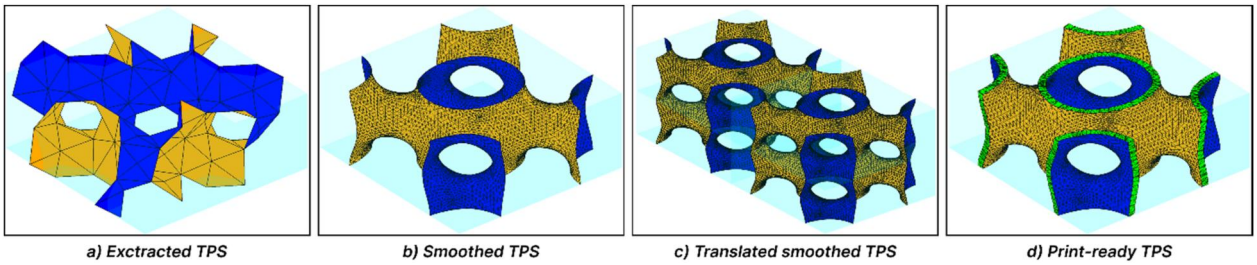

Figure 5. Generated TPS from Co-Ga-P-5 zeolite (CGF) before and after processing with porous 3D. a) Extracted from ToposPro CGF TPS. b) Smoothed CGF TPS. c) Translated and smoothed CGF TPS. d) Print-ready CGF TPS.

Figure 6 presents the simulated von Mises stress distribution patterns across the samples. The results demonstrate generally uniform stress distribution with limited high-stress concentration areas. The BRE structure shows particularly notable behavior, exhibiting exceptionally low stress concentrations. In contrast, several structures display more pronounced high-stress regions, including ITW, LAU, RHO, SOD (Schwarz P-surface), and UEI configurations.

The elastic parameters of the RVEs for porous structures in Table 2 were obtained using a model where steel was specified as the base material. To extend the applicability of these calculations – i.e. to assess the elastic properties of porous structures made from materials other than steel – a Gibson-Ashby analysis was performed So, the analysis of the compression moduli E_{33} for the porous structure unit cells shown in Figure 6 are presented on Figure 7 according to the Gibson-Ashby dependence [34]:

$$\frac{P^*}{P_{mat}} = \left(\frac{\rho^*}{\rho_{mat}}\right)^{\alpha}, \tag{1}$$

where P^* is Young's modulus or shear modulus of the porous structure, P_{mat} is the corresponding value of the initial material, ρ^* is the average density of the porous material, ρ_{mat} is the density of the initial material, α is a parameter

Table 2. Normalized elastic moduli and Poisson's ratios of triply periodic P-surface porous structures fabricated from structural steel [32].

TPS	E_{11}/E_{mat}	E_{22}/E_{mat}	E_{33}/E_{mat}	G_{12}/G_{mat}	G_{23}/G_{mat}	G_{31}/G_{mat}	ν_{12}	ν_{23}	ν_{31}
SOD	0.026	0.026	0.026	0.029	0.029	0.029	0.366	0.366	0.366
RHO	0.026	0.026	0.026	0.027	0.027	0.027	0.367	0.367	0.367
LTA	0.073	0.073	0.073	0.027	0.027	0.027	0.223	0.223	0.223
ATN	0.012	0.012	0.073	0.043	0.029	0.029	0.529	0.518	0.518
MER	0.036	0.036	0.069	0.088	0.071	0.071	0.434	0.133	0.133
SAS	0.026	0.026	0.089	0.082	0.069	0.069	0.448	0.131	0.131
BCT	0.028	0.028	0.082	0.089	0.064	0.064	0.476	0.148	0.148
JSW	0.043	0.047	0.090	0.070	0.047	0.047	0.184	0.174	0.341
HEU	0.031	0.039	0.167	0.069	0.045	0.043	0.151	0.251	0.143
CGF	0.001	0.001	0.100	0.058	0.001	0.001	0.193	0.348	0.348
ITW	0.001	0.068	0.070	0.060	0.002	0.034	0.234	0.391	0.396
EDI	0.017	0.018	0.164	0.105	0.042	0.044	0.241	0.259	0.388
UEI	0.019	0.029	0.058	0.053	0.015	0.028	0.186	0.347	0.527
BRE	0.012	0.031	0.052	0.026	0.015	0.032	0.183	0.129	0.530
LAU	0.051	0.060	0.077	0.043	0.074	0.076	0.215	0.485	0.679

Bulk material properties: Young's modulus $e_{mat} = 200$ GPa, shear modulus $g_{mat} = 76.92$ GPa, and poisson's ratio $\nu_{mat} = 0.33$.

that depends only on the geometrical-topological properties of the porous material.

As evidenced in Figure 7, the logarithmic plots demonstrate strictly linear scaling behavior with parallel trendlines for all porous structures, confirming the ratio of their mechanical properties to be invariant across the studied density range. The complete set of Gibson-Ashby scaling relations for all other elastic moduli and Poisson's ratios from Table 2 can be found in Appendix A.

Table 3 presents the geometric characteristics of the porous structures listed in Table 2. The porosity φ was calculated as follows:

$$\varphi = \left(1 - \frac{V_{str}}{V_{cell}}\right) \cdot 100, \tag{2}$$

where V_{str} is the solid framework volume and V_{cell} is the enclosing cube volume [43].

Table 3 demonstrates that the P-frameworks maintain exceptionally high porosity even with a 2 mm wall thickness. However, both this parameter and pore dimensions can be varied within the limits constrained by topological preservation, specifically, avoiding structural anomalies like self-intersections. Notably, pore sizes can be systematically reduced to produce candidate structures suitable for bone implant applications [10].

As established in our earlier discussion of Table 2, the majority of TPS(P)-based structures in this study demonstrate a significantly higher compression resistance along the z-axis compared to other directions, while showing no strong dependence in their shear moduli. For a detailed investigation, we have focused on three particularly z-axis-resistant configurations: CGF, HEU, and SAS.

The HEU structure displays pronounced mechanical anisotropy across all three principal axes, emerging as the stiffest configuration under compressive loading in any direction. Its compression and shear moduli substantially exceed those of the reference SOD structure (Schwarz P-surface) in all measured parameters. In contrast, the CGF material exhibits isotropic behavior under x- and y-axis compression, recording the lowest in-plane moduli among all studied structures (with the only exception of ITW's E_{11} value). This structure demonstrates extreme z-axis dominance, with its longitudinal compression modulus surpassing transverse values by about 100 times, while simultaneously showing the lowest shear moduli (G_{23} and G_{31}) in our dataset. The SAS structure presents an intermediate case, closely matching the SOD configuration's behavior under x- and y-axis compression while outperforming it significantly in all other mechanical properties.

These selected representative structures span the spectrum from full anisotropy (HEU) through extreme unidirectional reinforcement (CGF) to modified conventional behavior (SAS) and form the basis for our subsequent investigation of more complex architectures in Section 4, where we analyze mechanical properties of porous structures constructed from their unit cells (Figure 2).

4. Finite element modeling of CGF-, HEU-, and SAS-based porous structures

Following the identification of mechanically promising CGF, HEU, and SAS unit cell configurations in Section 3 (Figure 6, Table 2), we performed detailed FE analysis of extended porous structures constructed from these unit cells. The complex architectures were generated by spatially replicating STL-modeled unit cells in $2 \times 2 \times 2$, $3 \times 3 \times 3$, and $4 \times 4 \times 4$ arrays along three orthogonal axes, preserving the original cellular dimensions established in Section 3. Numerical simulations were implemented in ANSYS 2018 R2 using PLA+ (due to its high stiffness compared to alternatives) parameters (Table 4) to match subsequent 3D printing requirements.

As was well-established, PLA+ plastic exhibits elastic-plastic behavior. Consequently, it is necessary to employ a multilinear isotropic plasticity model to accurately represent the material's mechanical response in our simulations. The corresponding multilinear isotropic hardening curve for PLA+ plastic used for this constitutive model is presented in Figure 8.

The unit cell geometries were initially designed in STL-format (Figure 9(a)). For FE analysis, each STL-model underwent reverse engineering conversion into surface bodies (Figure 9(b)), which were then stitched to form solid volumetric representations (Figure 9(c)). These solid frames were subsequently replicated and spatially arranged along

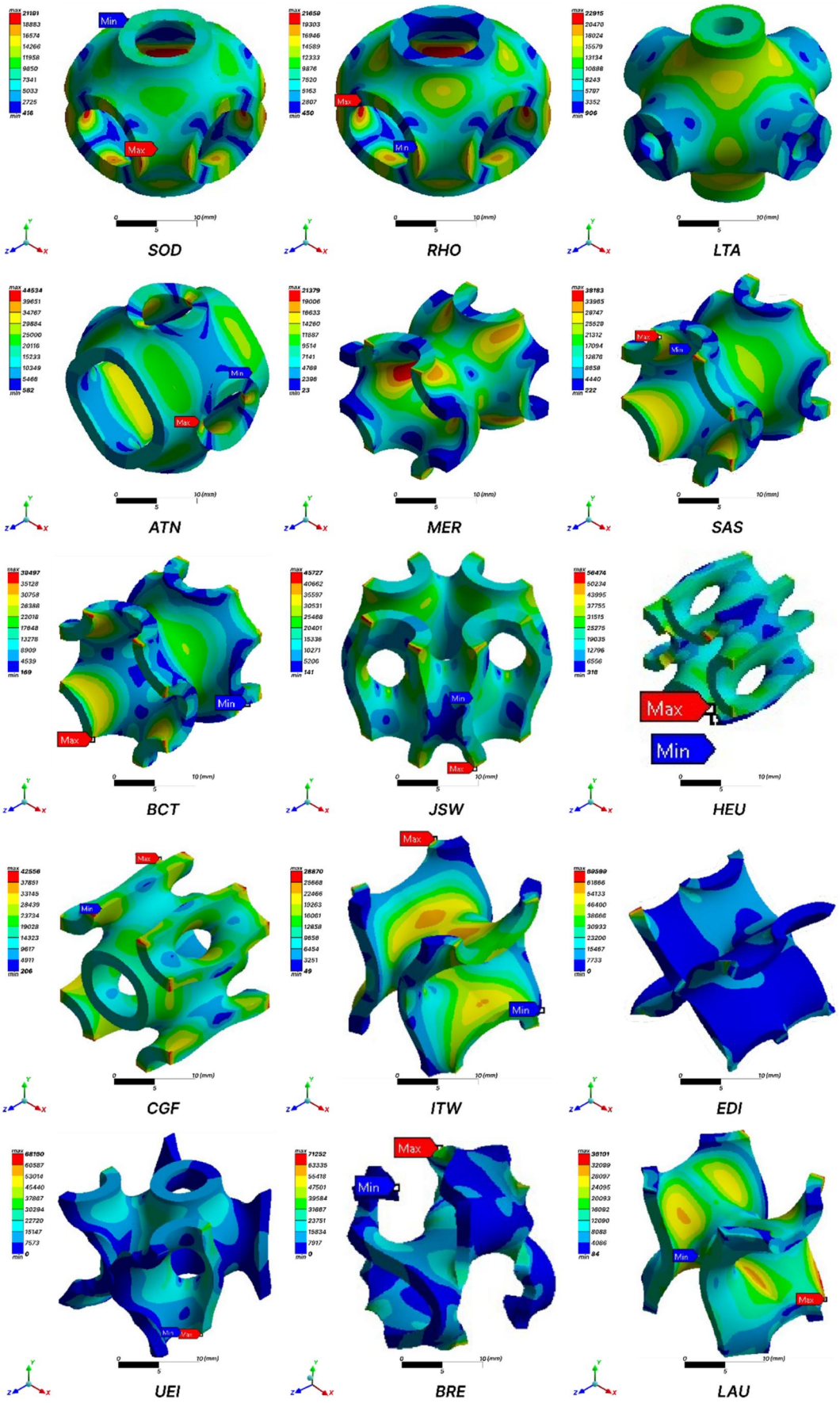

Figure 6. Von mises stress distribution in RVEs of 15 TPS(P)s from Table 2.

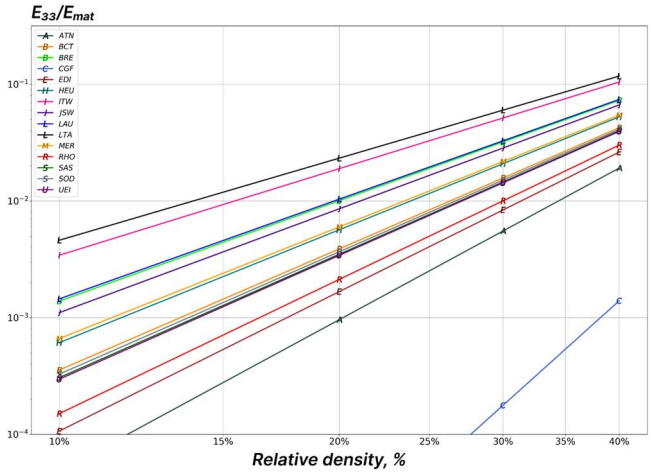

Figure 7. Logarithmic-scale plot of normalized compression moduli E_{33}/e_{mat} *versus* relative density (1) for unit cells of porous structures (Table 2 and Figure 3).

Table 3. Geometrical properties of porous structure unit cells (Figure 2).

RVE	S_{surf}, mm^2	Porosity, %
SOD	940.15	97.65
RHO	937.76	97.66
LTA	784.56	98.04
ATN	976.27	97.57
MER	939.97	97.66
SAS	946.18	97.64
BCT	940.21	97.66
JSW	1252.5	96.90
HEU	1317.9	96.73
CGF	1318.6	96.71
ITW	968.92	97.58
EDI	982.15	97.79
UEI	1252.6	96.90
BRE	1026.0	97.45
LAU	983.21	97.55

S_{surf} is surface area per unit cell, wall thickness is 2 mm (uniform).

Table 4. Mechanical parameters of post-processed PLA+ material.

Parameters	Units	Values
Density	g/cm^3	1.24
Compression modulus, E_{mat}	MPa	2000
Poisson's ratio, ν_{mat}		0.36
Yield strength, $\sigma_{Y,}$	MPa	60
Compressive strength, σ_{US}	MPa	70
Elongation at break	%	8

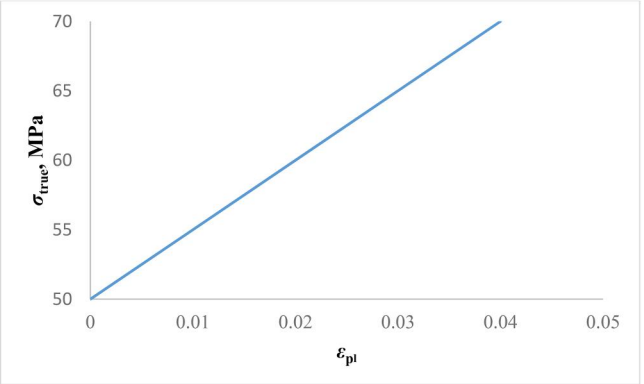

Figure 8. Multilinear isotropic hardening curve for PLA+ plastic. ε_{pl} is the relative plastic strain, σ_{true} is true stress.

three orthogonal axes (Figure 9(d)), culminating in a fully integrated geometric assembly (Figure 9(e)).

For enhanced surface smoothing, we employed virtual topology processing (Figure 9(f)). While more computationally intensive than implicit TPMS generation methods [44], this approach yields superior surface quality to be essential for high-fidelity simulations.

To improve the modeling of plasticity during sample compression, the nonlinear mechanics option was enabled. This allowed us to use a finer FE mesh on the faces where the unit cells are stitched together, providing more accurate modeling of nonlinear deformation processes. The SOLID98 element type [32] was used for the FE analysis, which is a tetrahedral element well-suited for accounting for geometric nonlinearity. The characteristic FE size was set to 1 mm.

During the compression simulation, each FE underwent deformation according to a uniaxial compression scenario. The position of the lower boundary of the samples was fixed in accordance with Dirichlet boundary conditions, while a Neumann condition was applied to the upper boundary corresponding to the imposed compressive force. Friction was not accounted for in the model. To enhance the modeling of plasticity during sample compression, the nonlinear mechanics option was activated. The convergence criteria for the computational procedure were set as follows: force tolerance – 0.5%, displacement tolerance – 5%, and energy tolerance – 0.1%. Standard error control strategies for nonlinear materials were employed. For mesh sensitivity analysis, h-adaptation based on the Zienkiewicz-Zhu method [54,55] was used, resulting in an additive FE mesh that ensures the specified computational accuracy.

The modeled mechanical properties of the porous structures are presented in Table 5. These computational results, alongside experimental validations in Section 5, establish relationships between topological design and mechanical performance in additively manufactured porous metamaterials. The methodology demonstrates how unit cell properties can be effectively translated to functional engineering-scale components while retaining designed anisotropic features.

As shown in Table 5, both HEU and CGF structures demonstrate increased yield strength under z-axis compression compared to the base material (Table 4). The CGF configurations show improvements of 4% ($2 \times 2 \times 2$ CGF and $4 \times 4 \times 4$ CGF) and 5.5% ($3 \times 3 \times 3$ CGF), while the HEU structures exhibit enhancements of 2.8% ($2 \times 2 \times 2$ HEU), 11% ($3 \times 3 \times 3$ HEU), and 13.5% ($4 \times 4 \times 4$ HEU).

The observed mechanical behavior of the studied structures can be explained through von Mises stress distribution patterns. Figure 10 presents the computed stress fields obtained from the described numerical model, revealing critical insights into the structures' performance.

Figure 10 clearly shows that in the SAS structure, the stresses primarily concentrate at internal junctions while remaining minimal at the pore boundaries. In contrast, CGF and HEU structures exhibit maximum stresses at protruding boundary features – precisely at the potential stitching regions where additional unit cells would connect during the structure expansion. During z-axis compression, internal

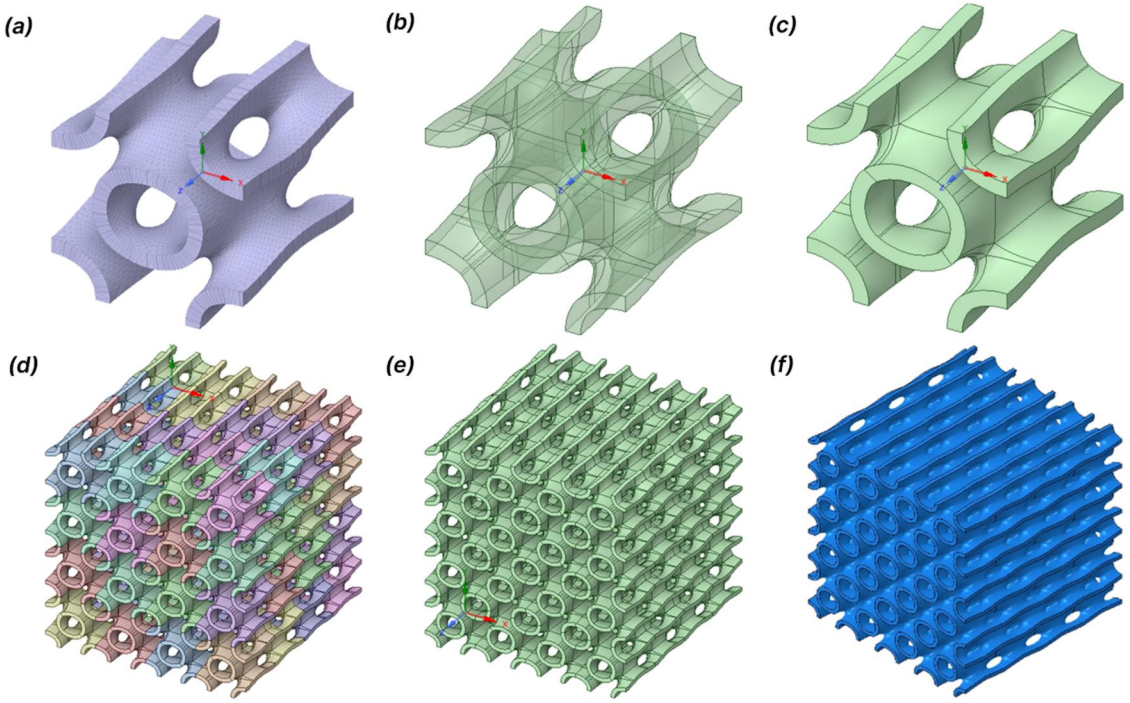

Figure 9. The procedure of geometric modeling in the FE method using the example of a porous CFG structure. (a) STL-model of CGF-structure, (b) transitioning from mesh data to surface body of CGF-structure, (c) solid body of CGF-structure, (d) $4 \times 4 \times 4$ geometrical assembly of STL-models of CGF-structure, (e) $4 \times 4 \times 4$ geometrical assembly of surface bodies of CGF-structure, and (f) $4 \times 4 \times 4$ geometrical assembly of solid bodies of CGF-structure.

Table 5. Mechanical properties of HEU-, CGF-, and SAS-type porous structures obtained by FE modeling.

Sample	Axis	TPS(P)	E_C, MPa	σ_Y, MPa	σ_{US}, MPa
$2 \times 2 \times 2$	x	CGF	805.10	27.53	39.01
		HEU	885.07	19.01	35.69
		SAS	337.36	24.47	24.48
	y	CGF	607.92	20.78	29.34
		HEU	959.80	20.60	37.50
		SAS	337.36	24.47	24.48
	z	CGF	1902.04	62.42	67.80
		HEU	1456.29	61.66	66.54
		SAS	1388.41	40.76	45.75
$3 \times 3 \times 3$	x	CGF	893.40	24.75	33.60
		HEU	981.52	17.09	30.74
		SAS	323.62	20.96	23.97
	y	CGF	844.14	23.65	32.26
		HEU	1332.75	23.45	41.23
		SAS	323.62	20.96	23.97
	z	CGF	1818.82	63.28	66.98
		HEU	1878.35	66.68	75.14
		SAS	1335.25	39.65	43.54
$4 \times 4 \times 4$	x	CGF	896.33	26.72	30.46
		HEU	984.74	18.45	27.87
		SAS	368.67	31.50	39.58
	y	CGF	840.43	25.19	28.72
		HEU	1326.89	24.97	36.71
		SAS	368.67	31.50	39.58
	z	CGF	1355.39	62.40	65.71
		HEU	1539.10	71.35	79.35
		SAS	1529.77	35.01	41.96

E_C is young's modulus, σ_Y is yield stress, σ_{US} is ultimate compressive strength.

areas of CGF and HEU maintain relatively low stress levels. This stress distribution directly influences the failure behavior. CGF and HEU structures should be failed progressively through boundary fractures while preserving its internal architecture intact. Since boundary damage minimally affects overall mechanical properties, this creates a strengthening effect, as evidenced by comparing strength limits in Tables 4 and 5. Conversely, SAS structures fail through internal fractures which immediately compromise the entire architecture, leading to failure at lower loads (Table 5). These computational predictions have been experimentally verified through physical testing (Section 5), confirming the relationship between stress localization patterns and structural performance. The findings demonstrate how topological design can be optimized to control failure modes and enhance mechanical properties in porous architectures.

The strengthening effects observed in CGF and HEU porous structures compared to the base material (Tables 4 and 5) can be further analyzed by examining the asymmetry of stress states, specifically the distribution of compressive and tensile stresses within the samples. For this purpose, we calculate the third invariant of the stress tensor I_3:

$$I_3 = det(\sigma_{ij}), \tag{3}$$

where σ_{11}, σ_{22}, and σ_{33} represent the normal stresses along the x, y, and z axes, respectively, while σ_{12}, σ_{23}, and σ_{31} denote the corresponding shear stress components.

The spatial distribution of the third stress invariant I_3 from Eq. (3) in the studied samples is presented in Figure 11.

The color scale in Figure 11 indicates that stress values close to zero are represented by bright green. The figure reveals that in the HEU porous structure, mechanical stresses near pore walls remain relatively low, with a similar but slightly less pronounced effect observed in the CGF structure. In contrast, the SAS structure experiences significantly higher stresses in these regions. These observations clearly illustrate the strengthening effect occurring in HEU and CGF structures, which is notably absent in SAS (see

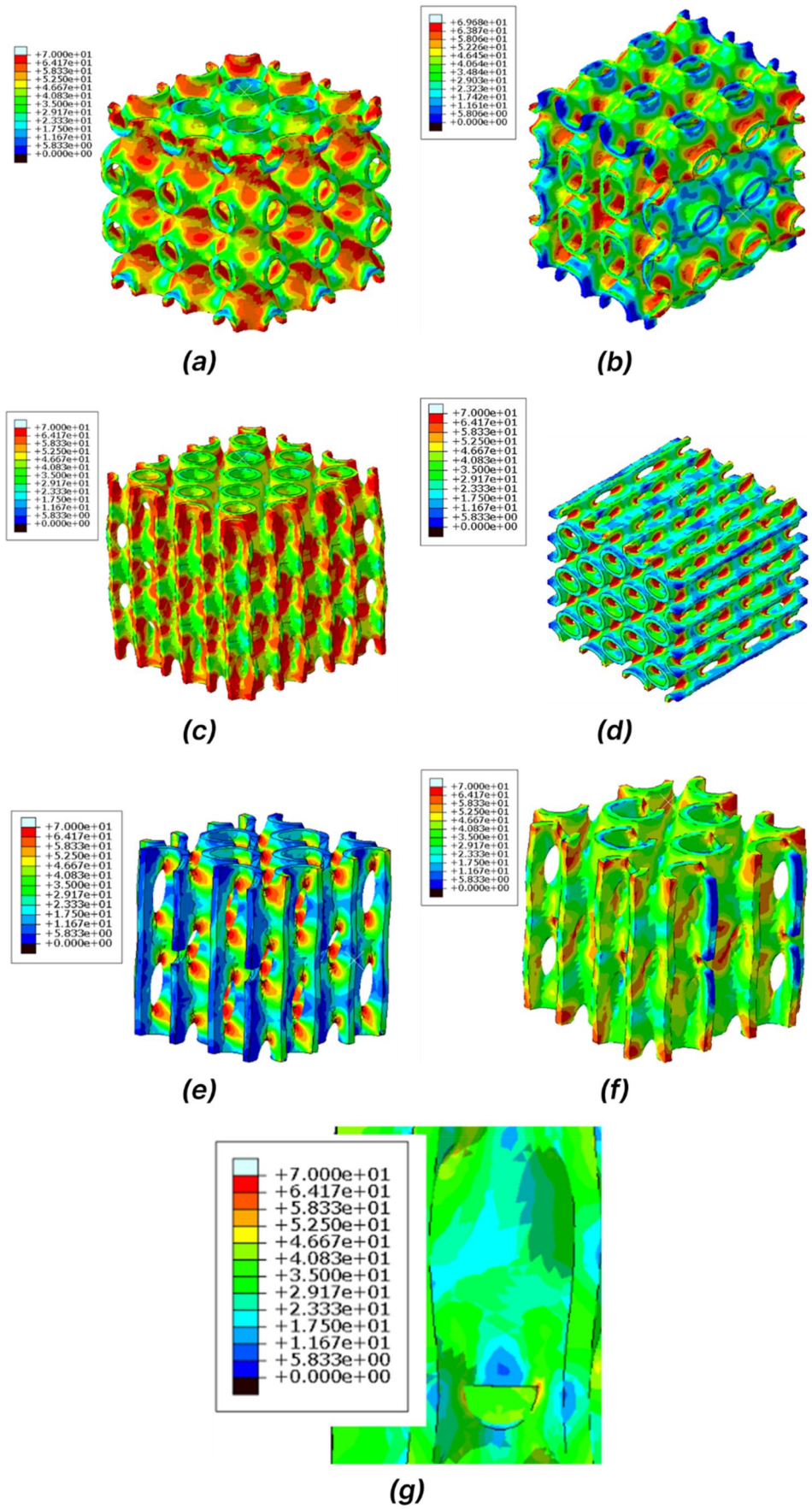

Figure 10. Von mises stress distribution in SAS (a – deformation on *z*-axis, b – deformation *x*-axis), CGF (c – deformation on *z*-axis, d – deformation *x*-axis) and HEU (e – deformation on *x*-axis, f – deformation *z*-axis), and g – von mises stress distribution at the boundary of HEU cells.

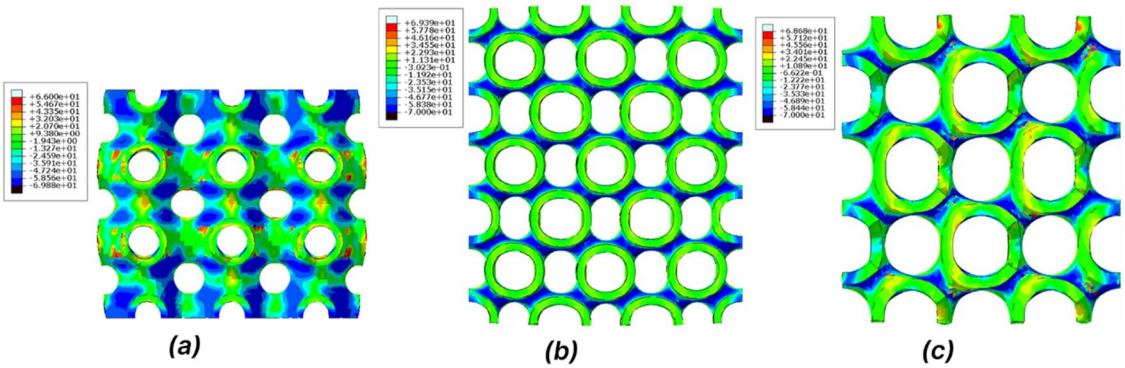

Figure 11. The distribution of the third stress tensor invariant I_3 from Eq. (3) under z-axis compression. (a) SAS-, (b) CGF-, and (c) HEU-structure.

Table 5). This demonstrates that creating porous materials based on P-surfaces (Table 1 and Figure 2) can, in certain cases, enhance the material's ultimate strength compared to the base solid material. The conclusions presented in this section are experimentally verified in Section 5 through comparative mechanical testing and failure analysis. The results confirm the relationship between stress distribution patterns and the observed strengthening effects in some architectural configurations.

5. Experimental investigation of SAS, CGF, and HEU porous structures

5.1. Additive manufacturing of SAS-, CGF-, and HEU-structures

For experimental investigation of the previously selected SAS, CGF, and HEU structures complex samples were fabricated using AM techniques. These specimens were produced from PLA+ plastic by stitching together corresponding STL-models of unit cells along three orthogonal directions, following the methodology described in Section 4 where their properties were numerically simulated. The mechanical parameters of the PLA+ material after passing through the printing device are presented in Table 4 and Figure 5.

The samples were printed using a Bambu Lab X1 Carbon 3D printer, with the specific printing parameters provided in Table 6.

The quality of 3D printing was controlled by optical methods. Figure 12 shows images obtained with an optical microscope for CGF, HEU, and SAS samples.

Based on the images in Figure 12, the quality of the printing of the pores and walls, which characterize the geometry of the frameworks, as well as the adhesion quality of the layers, can be assessed. It is evident that the SAS, CGF, and HEU frameworks exhibit dense and high-quality layering in the upper sections (Figure 12(a–c)). The layer thickness also shows a sufficiently high-quality microstructure, although some inclusions of string sludge are present (Figure 12(e,f)). Additionally, defects are observed in the uppermost layers of the components, which is a common issue in 3D printing and is attributed to the overheating of the extruder (Figure 12(d)). However, it is important to note that the defects identified through optical methods are isolated and do not critically affect the mechanical properties of the examined samples.

Table 6. Specific printing parameters of bambu lab X1 carbon 3D printer used to manufacture samples.

Parameters	Units	Values
Nozzle temperature	°C	220
Printing speed	mm/sec	200
Infill speed	mm/sec	300
Layer height	mm	0.16
Infill density	%	100
Build plate temperature	°C	42

5.2. Compression tests of SAS-, CGF-, and HEU-structures

Uniaxial compression tests of SAS, HEU, and CGF lattice structures made of PLA+ plastic were performed on an IR 5143-200 200 kN testing machine. A compressive force of 10 N was applied at room temperature with a constant deformation rate of 2 mm/min, corresponding to an axial strain rate of $0.001\,s^{-1}$. The appearance of the samples after compression is shown in Figure 13.

Figure 13 reveals residual deformations and signs of failure in the tested structures. The experimental results confirm the conclusions drawn in Section 4 based on the numerical modeling of the mechanical properties of the samples. Specifically, we observed failures occurring at the protruding boundary areas of the CGF and HEU structures, aligning with the stress distribution according to the von Mises criterion (Figure 10). In contrast, the boundary failures in the SAS structure are considerably less pronounced, with more extensive failures occurring in the internal regions, resulting in the samples breaking under lower loads.

5.3. Results of compression tests

The experimental loading curves are depicted in Figure 14. The loading values on the curve were measured with an accuracy of 1%.

The experimental results confirm the conclusions drawn in Section 4 based on the numerical modeling of the mechanical properties of the samples. Specifically, we observed failures occurring at the protruding boundary areas of the CGF and HEU structures, aligning with the stress

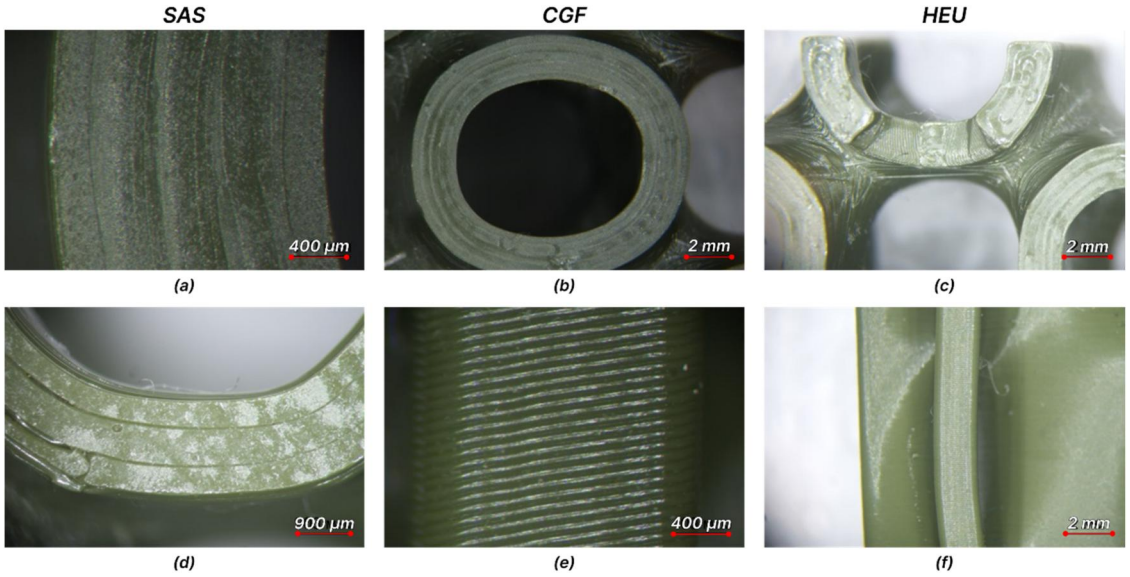

Figure 12. Optical microscopy images of 3D-printed SAS, CGF, and HEU porous structures with different magnification: (a) top-view of SAS-structure, (d) bottom-view of SAS-structure, (b) top-view of CGF-structure, (e) side-view of CGF-structure, (c) top-view of HEU-structure, and (f) side-view of HEU-structure.

distribution according to the von Mises criterion (Figure 10). In contrast, the boundary failures in the SAS structure are considerably less pronounced, with more extensive failures occurring in the internal regions, resulting in the samples breaking under lower loads.

Figure 14 shows that the loading curves for all tested samples demonstrate a smooth transition without abrupt changes. The curves feature a clearly defined linear region preceding the compressive yield point, followed by a short plastic deformation phase before reaching the compressive strength limit, after which the ultimate strength is attained immediately. The HEU $2 \times 2 \times 2$ sample shows the lowest stiffness among the tested samples. It is noteworthy to mention that the SAS structure, whose compression properties are closer to those of SOD compared to CGF and HEU (Table 2), fails at stresses significantly lower than the yield strength and tensile strength of the original PLA+ material. The behavior of the HEU and CGF structures under compression is particularly interesting. Firstly, linear deformations for these samples occur at stresses exceeding the yield strength of the original material. For instance, the yield strength of the CGF $2 \times 2 \times 2$ sample is 66.20 ± 0.66 MPa, which exceeds the yield strength of PLA+ by approximately 10%. Linear deformations are observed up to this loading value. For the HEU $3 \times 3 \times 3$ and HEU $4 \times 4 \times 4$ samples, linear deformations persist almost until the loading value corresponding to the ultimate strength of the original material, with observed ultimate strength values of 73.96 ± 0.74 MPa and 75.64 ± 0.76 MPa, respectively, which are about 6% and 8% higher than the ultimate strength of PLA+. The extended linear deformation regions and high ultimate strength in the CGF and HEU structures can likely be attributed to the low stress concentration in internal RVEs (as shown in Figures 10 and 11). It is important to note that the exceedance of the yield and strength limits of the porous CGF and HEU structures over the corresponding values for the original material (Figure 8) is significantly greater than the relative error in our compression experiments, indicating that these results are statistically significant.

The mechanical parameters of the samples, calculated from the experimental loading curve, are presented in Table 7.

It is noteworthy that the experimental values presented in Table 7 are in good agreement with the results of the numerical modeling conducted in Section 4 (Table 5). Thus, the porous structures based on TPS(P) of the HEU and CGF types exhibit strengthening properties compared to the characteristics of the original solid material. They show significant potential for creating structures with optimal mechanical properties and relative density, as well as for developing composites based on interpenetrating phases (IPC) [45].

5.4. Comparison of mechanical properties of SAS-, CGF-, and HEU-structures with mechanical properties of known structures

The Gibson-Ashby model [46] was used for comparison of our results for mechanical properties SAS-, CGF-, and HEU-structures with that of well-known TPS/TPMS. This model predicts the properties of cellular structure based on their relative density. Equations (1) and (2) show Gibson-Ashby's formulae for Young's modulus and yield strength. We employed formulas from the Gibson and Ashby [46] that are similar to Eq. (1):

$$\frac{E^*}{E_0} = C_1 \left(\frac{\rho^*}{\rho_0}\right)^{n_1}, \tag{4}$$

$$\frac{\sigma^*}{\sigma_0} = C_5 \left(\frac{\rho^*}{\rho_0}\right)^{n_5}, \tag{5}$$

where σ^* is the yield strength of the porous structure, σ_0 is

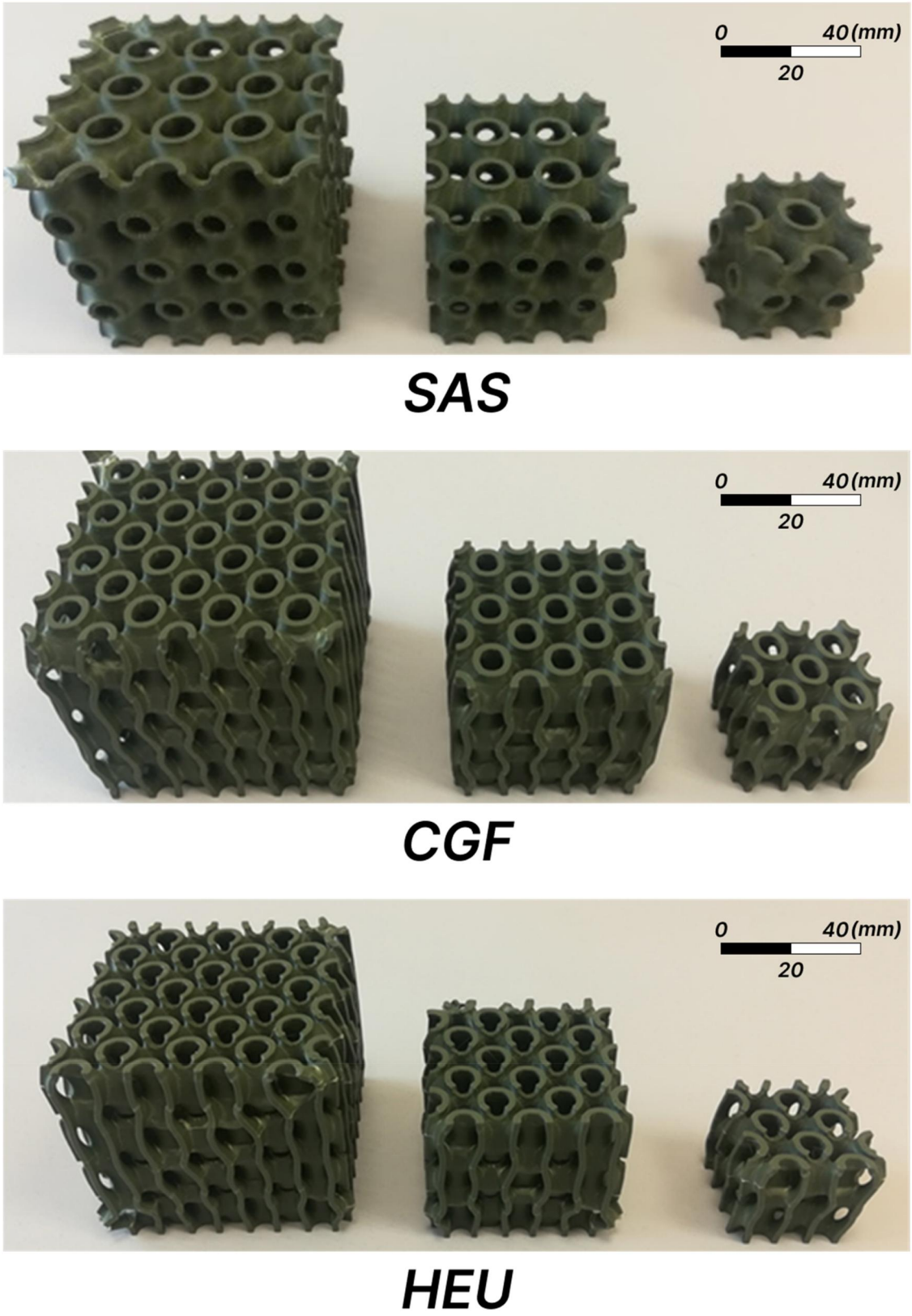

Figure 13. The samples of the CGF, HEU, and SAS structures after compression. In the HEU and CGF structures, damage is evident at the boundaries, while the internal points remain intact in corresponding with Figures 7 and 8.

the yield strength of the base material; C_1, C_5, n_1, n_5 are parameters determined experimentally.

For our comparative analysis, we rely on Laban et al. [47], which demonstrates that the general patterns of compression deformation show remarkable similarities between metal and polymer lattice structures. The principal distinction lies in the significantly higher load-bearing capacity of metal frameworks, attributable to their superior

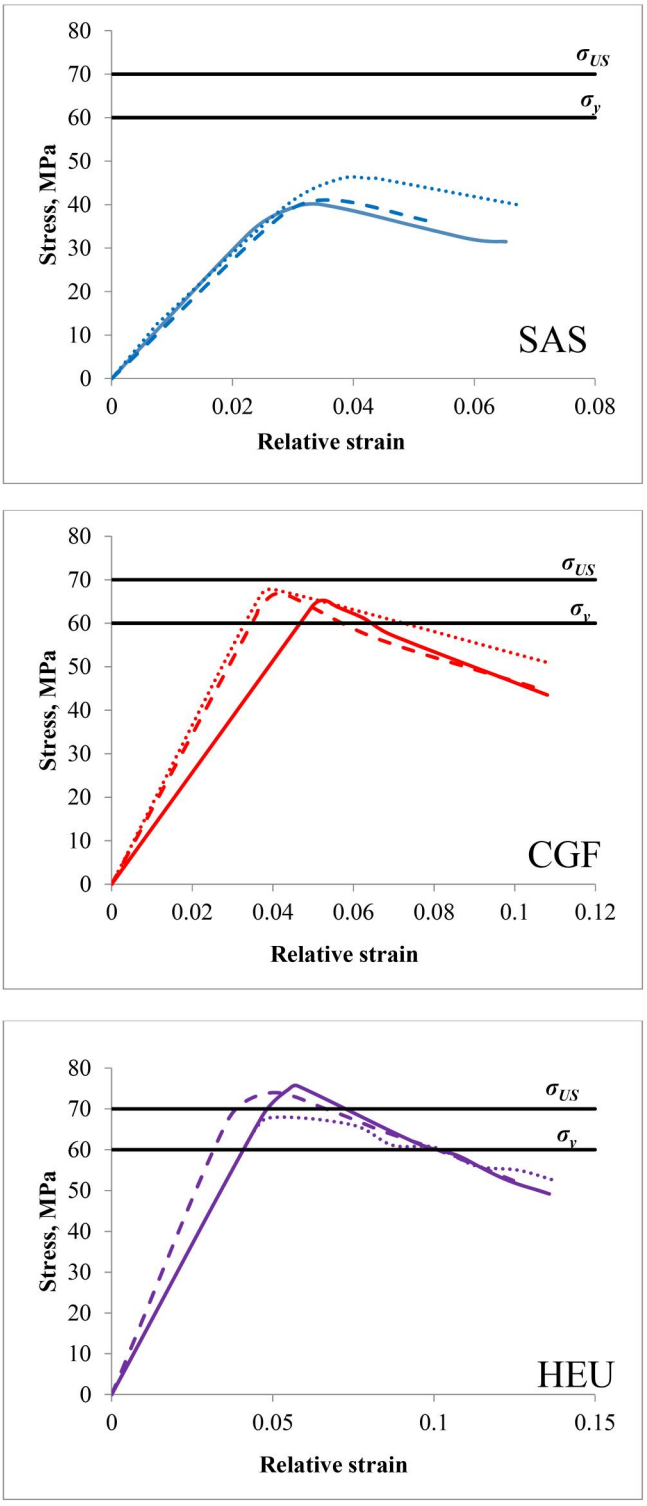

Figure 14. Stress-strain curves of PLA+-based HEU, CGF, and SAS porous structures under compression along *z*-axis. σ_Y is yield strength of PLA+, σ_{US} is ultimate strength of PLA+ (Table 4). Solid lines are 4 × 4 × 4 samples, dashed lines are 3 × 3 × 3 samples and dotted lines are 2 × 2 × 2 samples. Stress measurement accuracy is 1%.

yield strength. Furthermore, polymer lattices exhibit a tendency for brittle fracture, while metal samples display extensive plastic deformation leading to ductile fracture characteristics. Notably, this behavior pattern precisely matches our experimental observations for PLA+ porous samples (Figure 11). Consequently, we present our uniaxial compression test results for SAS-, CGF-, and HEU-structures in Figure 15 alongside a comprehensive compilation of experimental data for metal lattice structures fabricated *via* selective laser melting (SLM) technology from reference [48].

Table 7. The mechanical characteristics of the structures, derived from the experimental loading curve (Figure 11).

Sample	TPS(P)	E_C, MPa	σ_Y, MPa	σ_{US}, MPa
2×2×2	HEU	1469.14 ± 14.64	61.10 ± 0.61	67.72 ± 0.68
	CGF	1800.56 ± 18.01	66.20 ± 0.66	67.21 ± 0.67
	SAS	1380.18 ± 13.80	39.68 ± 0.40	46.07 ± 0.46
3×3×3	HEU	1865.50 ± 18.66	67.24 ± 0.67	73.96 ± 0.74
	CGF	1725.28 ± 17.26	63.37 ± 0.64	66.76 ± 0.67
	SAS	1279.43 ± 12.80	37.21 ± 0.37	41.04 ± 0.41
4×4×4	HEU	1460.25 ± 14.61	68.08 ± 0.68	75.64 ± 0.76
	CGF	1283.56 ± 12.84	64.72 ± 0.65	65.25 ± 0.66
	SAS	1469.52 ± 14.70	33.44 ± 0.34	40.00 ± 0.40

E_C is the compression modulus, σ_Y is yield strength, and σ_{US} is compressive strength. The measurement errors are 1%.

It is noteworthy that the compression modulus and yield strength of our CGF and HEU structures fabricated from plastic demonstrate comparability with corresponding parameters of metal-based structures.

6. Conclusion

This study presents a comparative investigation of porous structures derived from 15 triply periodic P-surfaces (TPS(P)). These P-surfaces were generated through the topological representation of atomic frameworks of zeolites. Numerical modeling of the mechanical properties of the porous structures was conducted, revealing structures that were more elastic and stronger than the materials from which they are fabricated. For instance, the yield strength of the CGF porous structure, produced from PLA+ plastic, exceeds that of the original material under compression along one of the axes by approximately 10%. Similarly, the ultimate strength of the HEU porous structure surpasses that of the original material by about 8%. The experimental validation of these strengthening effects is statistically significant.

The newly discovered triply periodic porous structures presented in this work open several promising research directions that merit deeper exploration. A critical avenue involves investigating how static mechanical properties depend on geometric parameters, particularly pore dimensions. Equally important would be complementing these static mechanical studies with dynamic characterization, especially of acoustic properties. Another significant research direction concerns developing IPCs by infiltrating the pores with polymers having different mechanical properties than the framework material. This approach could yield novel composite materials with tailored performance characteristics. Furthermore, the mechanical properties of related porous structures based on G- and D-type surfaces derived from zeolite atomic frameworks represent a natural extension of this work. Such studies would provide a more comprehensive understanding of structure-property relationships across different TPMS geometries. These investigations would advance both

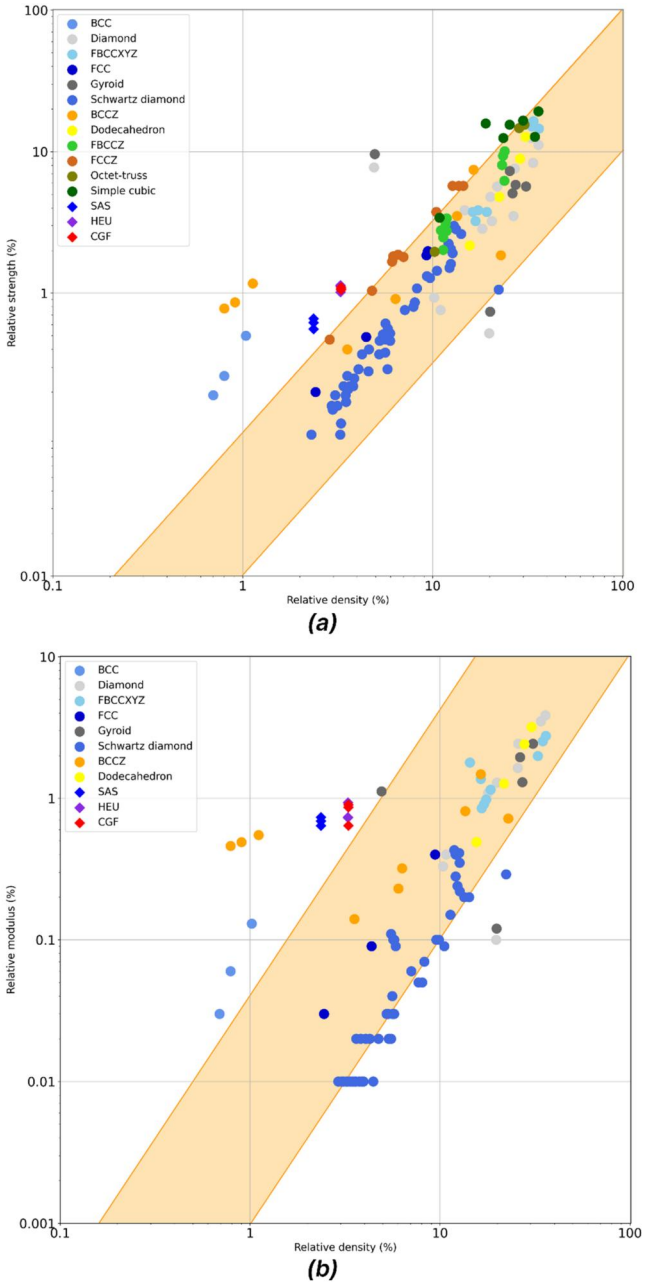

Figure 15. Summary of comparison between experimental data and the Gibson-Ashby model for (a) compressive strength and (b) Young's modulus. Multi-colored dots are values taken from sources [49–52], where BCC: BCC lattice structures; Diamond: Diamond skeletal-TPMS based cellular structures, FBCCXYZ: FCC lattice structure combined with BCCZ (BCC combined with Z struts) lattice structure with X- and Y-structures; FCC: FCC lattice structure; Gyroid: Gyroid structure, Schwartz diamond: Schwartz Diamond structure; BCCZ: BCC lattice combined with Z struts; dodecahedron: dodecahedron surface; FBCCZ: FCC lattice structure combined with BCCZ; FCCZ: FCC with Z-structures, octet-truss – lattice structure, simple cubic – lattice structure [53]. Multi-colored diamonds are the values obtained in this work.

fundamental knowledge and potential applications of these porous materials, particularly in areas requiring optimized mechanical performance and multifunctional material systems. The zeolite-inspired approach to TPMS generation offers rich opportunities for developing new materials with precisely controlled pore architectures.

The abundance of TPS/TPMS configurations generated by our approach presents both an intriguing and challenging problem: selecting the most suitable TPS structure for a given application. This raises fundamental questions about correlating topological/geometrical features with functional properties (e.g. mechanical behavior) of triply periodic structures. A particularly compelling aspect is the determination of relative contributions of surface topology/geometry *versus* bulk material properties in governing mechanical performance.

Disclosure statement

The authors report there are no competing interests to declare.

Funding

The research was supported by the Russian Science Foundation (grant No. 25-23-00123, https://rscf.ru/project/25-23-00123/).

References

[1] Z. Li, Z. Chen, X. Chen, and R. Zhao, Mechanical properties of triply periodic minimal surface (TPMS) scaffolds: considering the influence of spatial angle and surface curvature, Biomech. Model. Mechanobiol., vol. 22, no. 2, pp. 541–560, 2023. DOI: 10.1007/s10237-022-01661-7.

[2] Z.-H. Lin, J.-H. Pan, and H.-Y. Li, Mechanical strength of triply periodic minimal surface lattices subjected to three-point bending, Polymers (Basel), vol. 14, no. 14, pp. 2885, 2022. DOI: 10.3390/polym14142885.

[3] N. Baghous, I. Barsoum, and R.K. Abu Al-Rub, Generalized yield surface for sheet-based triply periodic minimal surface lattices, Int J. Mech Sci., vol. 252, pp. 108370, 2023. DOI: 10.1016/j.ijmecsci.2023.108370.

[4] Y. Wang, Y. Lian, Z. Wang, C. Wang, and D. Fang, A novel triple periodic minimal surface-like plate lattice and its data-driven optimization method for superior mechanical properties, Appl. Math. Mech.-Engl. Ed., vol. 45, no. 2, pp. 217–238, 2024. DOI: 10.1007/s10483-024-3079-7.

[5] Z. Wang, X. Wang, T. Gao, and C. Shi, Mechanical behavior and deformation mechanism of triply periodic minimal surface sheet under compressive loading, Mech. Adv. Mater. Struct., vol. 28, no. 19, pp. 2057–2069, 2021. DOI: 10.1080/15376494.2020.1829756.

[6] K. Yeranee, and Y. Rao, A review of recent investigations on flow and heat transfer enhancement in cooling channels embedded with triply periodic minimal surfaces (TPMS), Energies (Basel), vol. 15, no. 23, pp. 8994, 2022. DOI: 10.3390/en15238994.

[7] Q. Xia, J. Zhu, Q. Yu, J. Kim, and Y. Li, Triply periodic minimal surfaces based topology optimization for the hydrodynamic and convective heat transfer, Commun. Nonlin. Sci. Numer Simul., vol. 131, pp. 107819, 2024. DOI: 10.1016/j.cnsns.2024.107819.

[8] I. Maskery, N.T. Aboulkhair, A.O. Aremu, C.J. Tuck, and I.A. Ashcroft, Compressive failure modes and energy absorption in additively manufactured double gyroid lattices, Addit Manuf., vol. 16, pp. 24–29, 2017. DOI: 10.1016/j.addma.2017.04.003.

[9] L. Wallat, M. Selzer, U. Wasmuth, F. Poehler, and B. Nestler, Energy absorption capability of graded and non-graded sheet-based gyroid structures fabricated by microcast processing, J. Mater. Res. Technol., vol. 21, pp. 1798–1810, 2022. DOI: 10.1016/j.jmrt.2022.09.093.

[10] N. Elenskaya, M. Tashkinov, I. Vindokurov, Y. Pirogova, and V.V. Silberschmidt, Understanding of trabecular-cortical transition zone: numerical and experimental assessment of multi-morphology scaffolds, J. Mech. Behav. Biomed. Mater., vol. 147, pp. 106146, 2023. DOI: 10.1016/j.jmbbm.2023.106146.

[11] F.S.L. Bobbert, K. Lietaert, A. A. Eftekhari, B. Pouran, S.M. Ahmadi, H. Weinans, and A.A. Zadpoor, Additively manufactured metallic porous biomaterials based on minimal surfaces: a

unique combination of topological, mechanical, and mass transport properties, Acta Biomater., vol. 53, pp. 572–584, 2017. DOI: 10.1016/j.actbio.2017.02.024.

[12] B. Yilmaz, Additive manufacturing and characterization of mathematically designed bone scaffolds based on triply periodic minimal surface lattices, Mech. Adv. Mater. Struct., vol. 31, no. 15, pp. 3492–3502, 2024. DOI: 10.1080/15376494.2023.2177913.

[13] H. Wang, Z. Shu, P. Chen, J. Su, H. Zhu, J. Jiang, C. Yan, J. Xiao, and Y. Shi, Laser powder bed fusion printed poly-ether-ether-ketone/bioactive glass composite scaffolds with dual-scale pores for enhanced osseointegration and bone ingrowth, Acta Biomater., vol. 189, pp. 605–620, 2024. DOI: 10.1016/j.actbio.2024.09.055.

[14] E. Khedri, H. r Karimi, M.R.M. Aliha, N. Nazemzadeh, B. Talebi, and R. Aleali, Tensile, flexural, and mode-I cracking behavior of interpenetrating phase composites (IPC), developed using additively manufactured PLA-based structures with different infill densities and epoxy resin polymer as matrix, Results Eng., vol. 22, pp. 102162, 2024. DOI: 10.1016/j.rineng.2024.102162.

[15] K. Jain, Z. Wang, L.D. Garma, E. Engel, G.C. Ciftci, C. Fager, P.A. Larsson, and L. Wågberg, 3D printable composites of modified cellulose fibers and conductive polymers and their use in wearable electronics, Appl. Mater. Today, vol. 30, pp. 101703, 2023. DOI: 10.1016/j.apmt.2022.101703.

[16] L.B. Maslov, Dynamic model of a periodic medium with double porosity, Mech. Solids, vol. 53, no. 2, pp. 184–194, 2018. DOI: 10.3103/S0025654418020097.

[17] B. Hanks, J. Berthel, M. Frecker, and T.W. Simpson, Mechanical properties of additively manufactured metal lattice structures: data review and design interface, Addit Manuf., vol. 35, pp. 101301, 2020. DOI: 10.1016/j.addma.2020.101301.

[18] A.I. Borovkov, L.B. Maslov, M.A. Zhmaylo, F.D. Tarasenko, and L.S. Nezhinskaya, Elastic proprties of additively produced metamaterials based on lattice structures, Mater. Phys. Mech., vol. 51 (7), pp. 42–62, 2023. DOI: 10.18149/MPM.5172023_6.

[19] S. Altamimi, D.-W. Lee, I. Barsoum, R. Rowshan, I.M. Jasiuk, and R.K. Abu Al-Rub, Stiffness, strength, anisotropy, and buckling of lattices derived from TPMS and Platonic and Archimedean solids, Mech. Adv. Mater. Struct., vol. 32, no. 1, pp. 79–106, 2025. DOI: 10.1080/15376494.2024.2340066.

[20] D. Rahmatabadi, K. Soltanmohammadi, M. Aberoumand, E. Soleyman, I. Ghasemi, M. Baniassadi, K. Abrinia, M. Bodaghi, and M. Baghani, 4D printing of porous PLA-TPU structures: effect of applied deformation, loading mode and infill pattern on the shape memory performance, Phys. Scr., vol. 99, no. 2, pp. 025013, 2024. DOI: 10.1088/1402-4896/ad1957.

[21] P. Honari, D. Rahmatabadi, A. Bayati, E. Rassi, I. Ghasemi, M. Baniassadi, M. Bodaghi, and M. Baghani, Simultaneous 4D printing and In-Situ foaming for tailoring shape memory behaviors in polylactic acid foams, Manuf. Lett., vol. 43, pp. 33–36, 2025. DOI: 10.1016/j.mfglet.2024.11.005.

[22] J. Pérez, A new golden age of minimal surfaces, Notices Am. Math. Soc., vol. 64, no. 04, pp. 347–358, 2017. DOI: 10.1090/noti1500.

[23] L.C. Felix, R. Ambekar, R.M. Tromer, C.F. Woellner, V. Rodrigues, P.M. Ajayan, C.S. Tiwary, and D.S. Galvao, Schwarzites and Triply Periodic Minimal Surfaces: From Pure Topology Mathematics to Macroscale Applications, Small, pp. 2400351–2400382, 2024. DOI: 10.1002/smll.202400351.

[24] M. Yu. Arsentev, E.I. Sysoev, A.I. Makogon, S.V. Balabanov, M.M. Sychev, M.H. Hammouri, and V.A. Moshnikov, High-throughput screening of 3D-printed architected materials inspired by crystal lattices: procedure, challenges, and mechanical properties, ACS Omega, vol. 8, no. 28, pp. 24865–24874, 2023. DOI: 10.1021/acsomega.3c00874.

[25] F.D. Castañeda, G. García-Acosta, D.A. Garzón-Alvarado, K. Márquez-Flórez, D.A. Quexada-Rodriguez, and M.A. Velasco, Design for the additive manufacturing of structural elements with cellular materials using Voronoi diagrams and Delaunay triangulations: biological and structural applications, Mech. Adv. Mater. Struct., vol. 31, no. 27, pp. 9550–9570, 2024. DOI: 10.1080/15376494.2023.2276837.

[26] Y. Xu, H. Pan, R. Wang, Q. Du, and L. Lu, New families of triply periodic minimal surface-like shell lattices, Addit Manuf., vol. 77, pp. 103779, 2023. DOI: 10.1016/j.addma.2023.103779.

[27] M.I. Smolkov, O.A. Blatova, A.F. Krutov, and V.A. Blatov, Generating triply periodic surfaces from crystal structures: the tiling approach and its application to zeolites, Acta Crystallogr. A Found Adv., vol. 78, no. Pt 4, pp. 327–336, 2022. DOI: 10.1107/S2053273322004545.

[28] C. Baerlocher, L.B. Mccusker, and D.H. Olson, Atlas of Zeolite Framework Types, Elsevier Science, Amsterdam, Netherlands, 2007. DOI: 10.1016/B978-0-444-53064-6.X5186-X.

[29] H. Li, M. Eddaoudi, M. O'Keeffe, and O.M. Yaghi, Design and synthesis of an exceptionally stable and highly porous metal-organic framework, Nature, vol. 402, no. 6759, pp. 276–279, 1999. DOI: 10.1038/46248.

[30] W. Fischer, and E. Koch, New surface patches for minimal balance surfaces. I. Branched catenoids, Acta Crystallogr. A Found Crystallogr., vol. 45, no. 2, pp. 166–169, 1989. DOI: 10.1107/S0108767388010797.

[31] V.A. Blatov, A.P. Shevchenko, and D.M. Proserpio, Applied topological analysis of crystal structures with the program package toposPro, Cryst. Growth Des., vol. 14, no. 7, pp. 3576–3586, 2014. DOI: 10.1021/cg500498k.

[32] M.K. Thompson, and J.M. Thompson, ANSYS Mechanical APDL for Finite Element Analysis, Butterworth-Heinemann, Oxford, 2017.

[33] A.V. Eremin, M.A. Frolov, A.F. Krutov, M.I. Smolkov, A.S. Shulga, D.M. Bragin, A.I. Popov, and V.A. Blatov, Mechanical properties of porous materials based on new triply periodic and minimal surfaces, Mech. Adv. Mater. Struct., vol. 31, no. 29, pp. 11320–11336, 2024. DOI: 10.1080/15376494.2024.2303724.

[34] M.F. Ashby, A. Evans, N. Fleck, L.J. Gibson, J.W. Hutchinson, H.N.G. Wadley, and F. Delale, Metal Foams: A Design Guide, Butterworth-Heinemann, Elsevier, Oxford, 2000. DOI: 10.1016/B978-0-7506-7219-1.X5000-4.

[35] M. O'Keeffe, Tiling by numbers, Nature, vol. 400, no. 6745, pp. 617–618, 1999. DOI: 10.1038/23139.

[36] O.D. Friedrichs, A.W.M. Dress, D.H. Huson, J. Klinowski, and A.L. Mackay, Systematic enumeration of crystalline networks, Nature, vol. 400, no. 6745, pp. 644–647, 1999. DOI: 10.1038/23210.

[37] V.A. Blatov, O. Delgado-Friedrichs, M. O'Keeffe, and D.M. Proserpio, Three-periodic nets and tilings: natural tilings for nets, Acta Crystallogr. A., vol. 63, no. Pt 5, pp. 418–425, 2007. DOI: 10.1107/S0108767307038287.

[38] Porous 3D, Samara, Russia: SCTMS. Available from https://p3d.topcryst.com/software/.

[39] D. Cohen-Steiner, and J.-M. Morvan, Restricted delaunay triangulations and normal cycle. In Proceedings of the Nineteenth Annual Symposium on Computational Geometry, ACM, New York, NY, pp. 312–321, 2003. DOI: 10.1145/777792.777839.

[40] ASME Boiler and Pressure Vessel Code, Section VIII, Division 2, Alternative Rules, Table 5-110.1, The American Society of Mechanical Engineers, New York, NY, 1998. Available from https://www.asme.org/codes-standards.

[41] V.S. Sufiiarov, A.V. Orlov, E.V. Borisov, V.V. Sokolova, M.O. Chukovenkova, A.V. Soklakov, D.S. Mikhaluk, and A.A. Popovich, Design and mechanical properties simulation of graded lattice structures for additive manufacturing endoprostheses, Mech. Adv. Mater. Struct., vol. 28, no. 16, pp. 1656–1662, 2021. DOI: 10.1080/15376494.2019.1700432.

[42] M.I. Smolkov, Triply periodic surface description using Laplace–Beltrami operator and a statistical ma-chine learning model, J. Samara State Tech. Univ. Ser. Phys. Math. Sci., vol. 29, no. 1, pp. 158–173, 2025. DOI: 10.14498/vsgtu2105.

[43] Y. Zeng, X. Du, H. Yao, P. Li, P. Dong, and J. Chen, An Nylon lattice structure with improved mechanical property and energy absorption capability, Compos. C Open Access., vol. 8, pp. 100285, Jul2022. DOI: 10.1016/j.jcomc.2022.100285.

[44] N. Khan, and A. Riccio, A systematic review of design for additive manufacturing of aerospace lattice structures: current

trends and future directions, Prog. Aerosp. Sci., vol. 149, pp. 101021, 2024. DOI: 10.1016/j.paerosci.2024.101021.
[45] O.C. Zienkiewicz, and J.Z. Zhu, The superconvergent patch recovery and a posteriori error estimates. Part 1: the recovery technique, Numer. Meth. Eng., vol. 33, no. 7, pp. 1331–1364, 1992. DOI: 10.1002/nme.1620330702.
[46] O.C. Zienkiewicz, and J.Z. Zhu, The superconvergent patch recovery and a posteriori error estimates. Part 2: error estimates and adaptivity, Numer. Meth. Eng., vol. 33, no. 7, pp. 1365–1382, 1992. DOI: 10.1002/nme.1620330703.
[47] N. Kota, M.S. Charan, T. Laha, and S. Roy, Review on development of metal/ceramic interpenetrating phase composites and critical analysis of their properties, Ceram Int., vol. 48, no. 2, pp. 1451–1483, 2022. DOI: 10.1016/j.ceramint.2021.09.232.
[48] L.J. Gibson, and M.F. Ashby, Cellular Solids, Cambridge University Press, Cambridge, 1997. DOI: 10.1017/CBO9781139878326.
[49] O. Laban, E. Mahdi, S. Samim, and J.-J. Cabibihan, A comparative study between polymer and metal additive manufacturing approaches in investigating stiffened hexagonal cells, Materials, vol. 14, no. 4, pp. 883, 2021. DOI: 10.3390/ma14040883.
[50] T. Maconachie, M. Leary, B. Lozanovski, X. Zhang, M. Qian, O. Faruque, and M. Brandt, SLM lattice structures: properties, performance, applications and challenges, Mater. Des., vol. 183, pp. 108137, 2019. DOI: 10.1016/j.matdes.2019.108137.
[51] O. Al-Ketan, R. Rowshan, and R.K. Abu Al-Rub, Topology-mechanical property relationship of 3D printed strut, skeletal, and sheet based periodic metallic cellular materials, Addit Manuf., vol. 19, pp. 167–183, Jan2018. DOI: 10.1016/j.addma.2017.12.006.
[52] C. Yan, L. Hao, A. Hussein, and P. Young, Ti–6Al–4V triply periodic minimal surface structures for bone implants fabricated via selective laser melting, J. Mech. Behav. Biomed. Mater., vol. 51, pp. 61–73, 2015. DOI: 10.1016/j.jmbbm.2015.06.024.
[53] C. Lu, C. Zhang, P. Wen, and F. Chen, Mechanical behavior of Al–Si10–Mg gyroid surface with variable topological parameters fabricated via laser powder bed fusion, J. Mater. Res. Technol., vol. 15, pp. 5650–5661, 2021. DOI: 10.1016/j.jmrt.2021.11.008.
[54] X. Guo, J. Ding, X. Li, S. Qu, X. Song, J.Y.H. Fuh, W.F. Lu, and W. Zhai, Enhancement in the mechanical behaviour of a Schwarz Primitive periodic minimal surface lattice structure design, Int. J. Mech. Sci., vol. 216, pp. 106977, 2022. DOI: 10.1016/j.ijmecsci.2021.106977.
[55] Y. Li, D. Jiang, R. Zhao, X. Wang, L. Wang, and L.-C. Zhang, High mechanical performance of lattice structures fabricated by additive manufacturing, Metals (Basel), vol. 14, no. 10, pp. 1165, Oct2024. DOI: 10.3390/met14101165.

Appendix A. Complete set of Gibson-Ashby scaling relations for all elastic moduli and Poisson's ratios of 15 TPSs

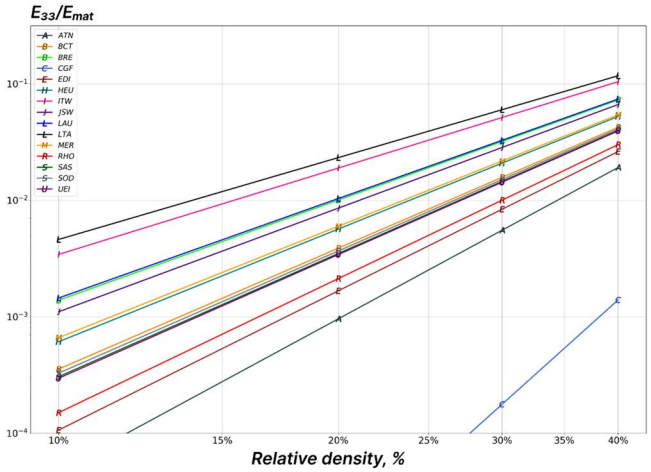

Figure A1. Logarithmic-scale plot of normalized compression moduli E_{33}/e_{mat} *versus* relative density (1) for RVEs of porous structures from Table 2 and Figure 3.

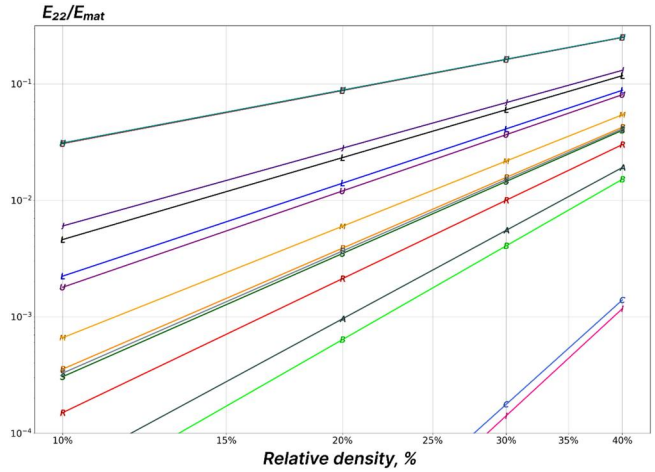

Figure A2. Logarithmic-scale plot of normalized compression moduli E_{22}/e_{mat} *versus* relative density (1) for RVEs of porous structures from Table 2 and Figure 3. Legend is the same as in Figure A1.

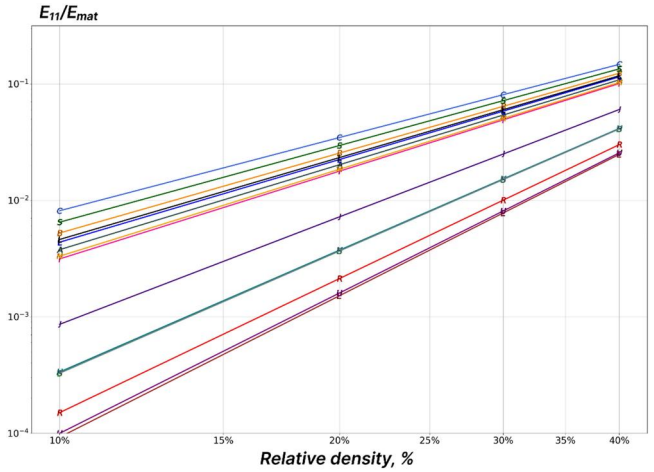

Figure A3. Logarithmic-scale plot of normalized compression moduli E_{11}/e_{mat} *versus* relative density (1) for RVEs of porous structures from Table 2 and Figure 3. Legend is the same as in Figure A1.

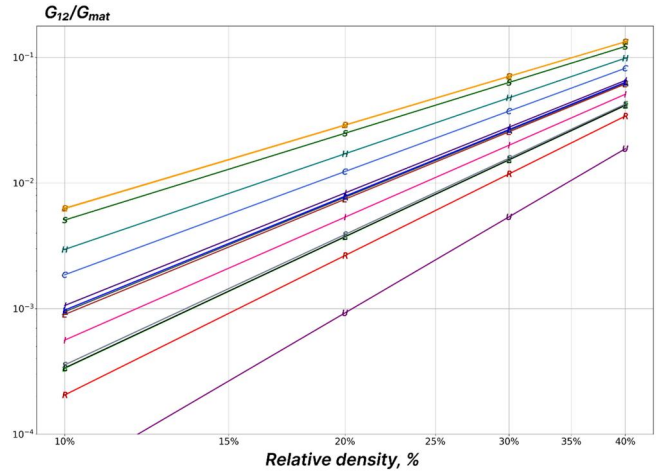

Figure A4. Logarithmic-scale plot of normalized shear moduli G_{12}/g_{mat} *versus* relative density (1) for RVEs of porous structures from Table 2 and Figure 3. Legend is the same as in Figure A1.

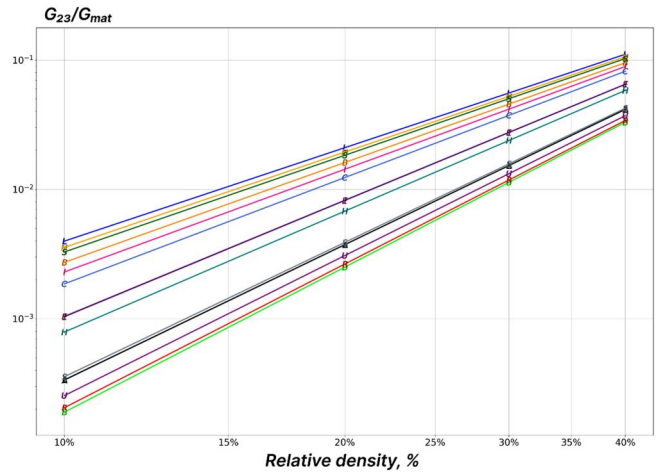

Figure A5. Logarithmic-scale plot of normalized shear moduli G_{23}/g_{mat} *versus* relative density (1) for RVEs of porous structures from Table 2 and Figure 3. Legend is the same as in Figure A1.

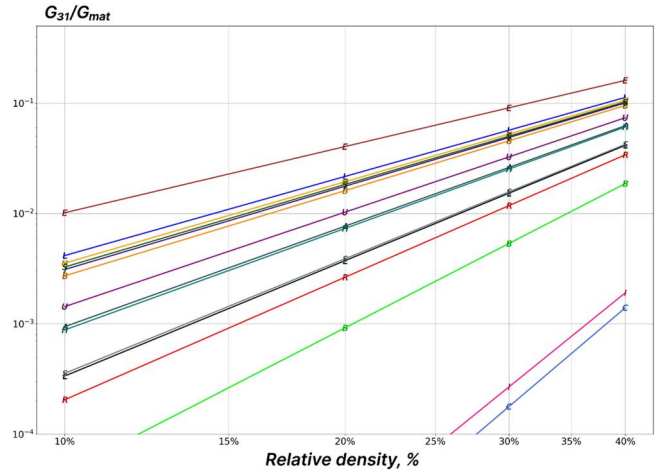

Figure A6. Logarithmic-scale plot of normalized shear moduli G_{31}/g_{mat} *versus* relative density (1) for RVEs of porous structures from Table 2 and Figure 3. Legend is the same as in Figure A1.

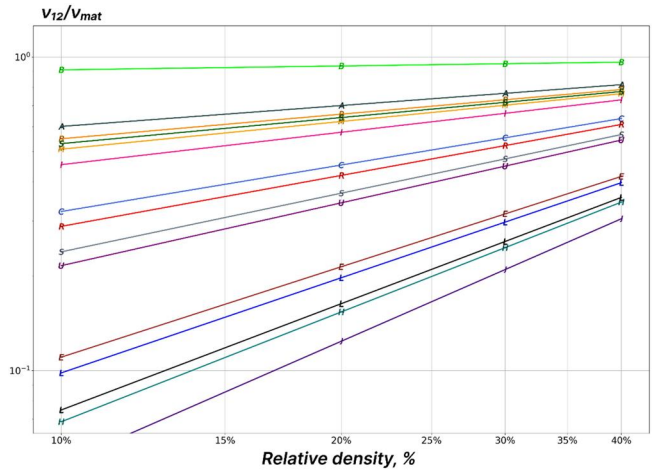

Figure A7. Logarithmic-scale plot of normalized Poisson's ratios ν_{12} *versus* relative density (1) for RVEs of porous structures from Table 2 and Figure 3. Legend is the same as in Figure A1.

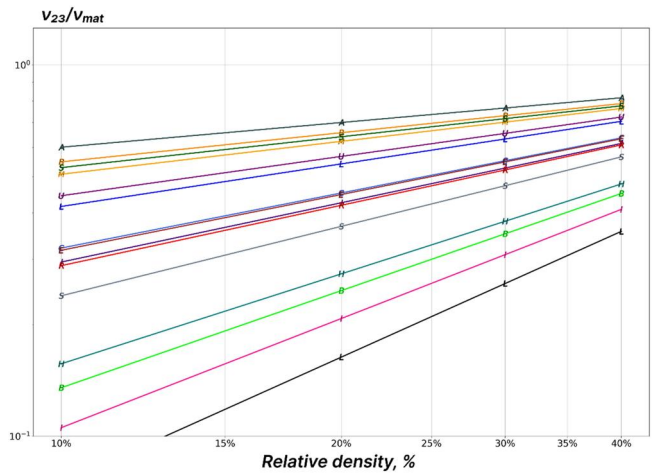

Figure A8. Logarithmic-scale plot of normalized Poisson's ratios ν_{23} *versus* relative density (1) for RVEs of porous structures from Table 2 and Figure 3. Legend is the same as in Figure A1.

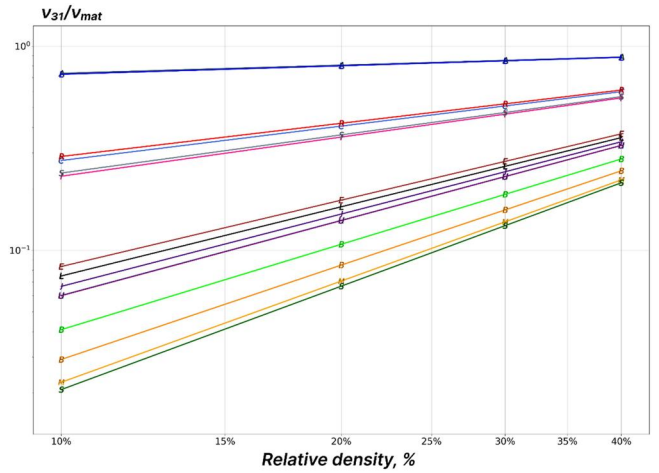

Figure A9. Logarithmic-scale plot of normalized Poisson's ratios ν_{31} *versus* relative density (1) for RVEs of porous structures from Table 2 and Figure 3. Legend is the same as in Figure A1.